

# Excitonic Bloch–Siegert shift in CsPbI<sub>3</sub> perovskite quantum dots

Received: 11 April 2022

Accepted: 13 September 2022

Published online: 22 September 2022

Check for updates

Yuxuan Li<sup>1,2</sup>, Yaoyao Han<sup>1,2</sup>, Wenfei Liang<sup>1</sup>, Boyu Zhang<sup>1,3</sup>, Yulu Li<sup>1</sup>, Yuan Liu<sup>1,4</sup>, Yupeng Yang<sup>1,2</sup>, Kaifeng Wu<sup>1,2</sup>✉ & Jingyi Zhu<sup>1</sup>✉

Coherent interaction between matter and light field induces both optical Stark effect and Bloch–Siegert shift. Observing the latter has been historically challenging, because it is weak and is often accompanied by a much stronger Stark shift. Herein, by controlling the light helicity, we can largely restrict these two effects to different spin-transitions in CsPbI<sub>3</sub> perovskite quantum dots, achieving room-temperature Bloch–Siegert shift as strong as 4 meV with near-infrared pulses. The ratio between the Bloch–Siegert and optical Stark shifts is however systematically higher than the prediction by the non-interacting, quasi-particle model. With a model that explicitly accounts for excitonic effects, we quantitatively reproduce the experimental observations. This model depicts a unified physical picture of the optical Stark effect, biexcitonic optical Stark effect and Bloch–Siegert shift in low-dimensional materials displaying strong many-body interactions, forming the basis for the implementation of these effects to information processing, optical modulation and Floquet engineering.

Quantum states of matter can be manipulated by applying intense light, examples of which include the famous optical Stark effect (OSE)<sup>1</sup> and Bloch–Siegert shift (BSS)<sup>2</sup> arising from coherent interactions between Floquet states<sup>3</sup> and equilibrium matter states. While originally observed in atomic/molecular systems, these effects have attracted strong attention in recent years for solid-state materials such as monolayer transition metal dichalcogenides (TMDs)<sup>4–7</sup> and lead halide perovskites<sup>8–10</sup>. Their strong light-matter interaction, in conjunction with spin-orbit coupling and/or symmetry breaking, allows for selective spin or valley state manipulation using the OSE. Moreover, the observation of a BSS, which has been historically intriguing due to its much weaker magnitude compared to the OSE, is now greatly eased thanks to the valley-exclusivity of these effects in monolayer TMDs under a quasi-particle representation<sup>11</sup>. Because the two time-reversed valleys  $K$  and  $K'$  are coupled to photons of opposite helicities, one can use helical light to pump at one valley and probe the BSS at the other one, which is naturally separated from the OSE that needs pump-

probe at the same valley. By pumping with infrared pulses, a valley-exclusive BSS with its magnitude approaching that of the OSE was demonstrated<sup>11</sup>.

Notably, the valley-exclusivity of the BSS and OSE reported in ref. 11 relies on a non-interacting quasi-particle approximation. On the other hand, however, recent studies on mono- and few-layer TMDs and many other low-dimensional material systems have in general found strong many-body interactions. These interactions induce strong excitonic and multiexcitonic effects, which will be generally called excitonic effects herein for simplicity. Under certain circumstances, the valley selection rules can be partially relaxed by excitonic effects. For example, in studies of monolayer TMDs<sup>12,13</sup> and CsPbBr<sub>3</sub> perovskite nanocrystals<sup>14</sup>, with small pump detuning energies of 10 s of meV, spectral modulations tunable from redshift, splitting to blueshift were observed when the pump and probe beams had opposite helicities, contradicting the simple expectation of a valley-selective OSE. This “anomalous” observation has been rationalized as a biexcitonic OSE in

<sup>1</sup>State Key Laboratory of Molecular Reaction Dynamics, Dalian Institute of Chemical Physics, Chinese Academy of Sciences, Dalian 116023 Liaoning, China.

<sup>2</sup>University of Chinese Academy of Sciences, 100049 Beijing, China. <sup>3</sup>Hubei Key Laboratory of Low Dimensional Optoelectronic Materials and Devices, Hubei University of Art and Science, Xiangyang 441053 Hubei, China. <sup>4</sup>University of Science and Technology of China, Hefei 230026 Anhui, China.

✉ e-mail: [kwu@dicp.ac.cn](mailto:kwu@dicp.ac.cn); [jingyizh@dicp.ac.cn](mailto:jingyizh@dicp.ac.cn)

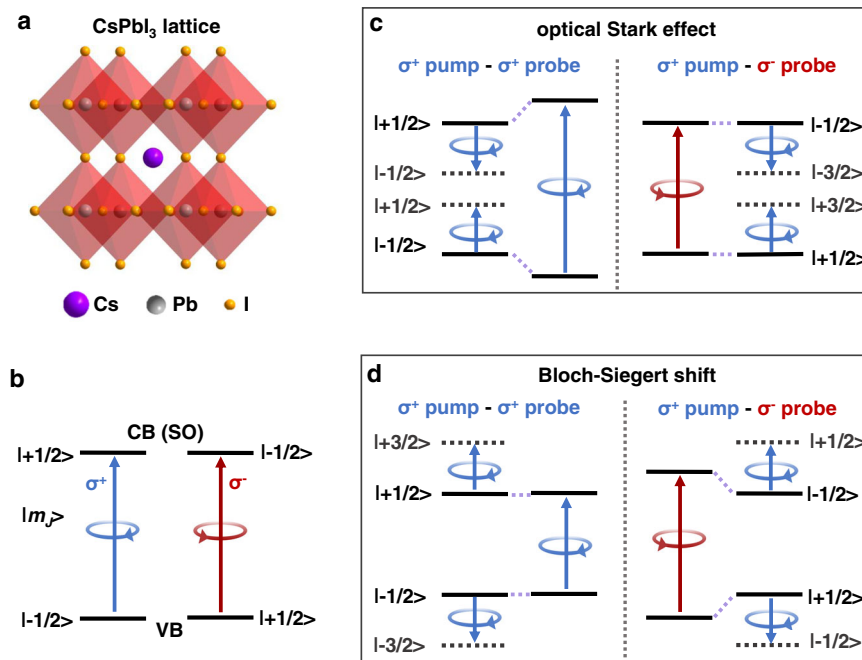


**Fig. 1 | Spin-selective transition rules and separation of the OSE and BSS in lead halide perovskites.** **a** Schematic illustration of the crystal structure of CsPbI<sub>3</sub> perovskite phase. **b** Conduction band (CB) and valence band (VB) edge states coupled to circularly-polarized photons. **c** Interaction energy diagram of the optical Stark shift driven by a nonresonant  $\sigma^+$  photon, which occurs at the VB  $| -1/2 \rangle$  and

CB  $| +1/2 \rangle$  states. The shift can be detected only with  $\sigma^+ \sigma^+$  pump-probe configuration. **d** Interaction energy diagram for the Bloch-Siegert shift driven by a non-resonant  $\sigma^+$  photon, which occurs at the VB  $| +1/2 \rangle$  and CB  $| -1/2 \rangle$  states and can be detected only with  $\sigma^+ \sigma^-$  pump-probe configuration.

which the single-exciton to biexciton transition plays an important role. So far, it remains unclear how these excitonic effects influence the valley- or spin-exclusivity of the BSS.

Here we report a strong BSS up to 4 meV in CsPbI<sub>3</sub> perovskite quantum dots (QDs) at room temperature. By controlling the light helicity, we can largely restrict the OSE and BSS to different angular momentum transitions and observe them separately, especially when the pump light is tuned from visible to infrared. Importantly, the ratio between the BSS and OSE magnitudes is significantly larger than the one predicted from a non-interacting, quasi-particle picture. By diagonalizing a  $9 \times 9$  Hamiltonian accounting for the co- and counter-rotating Floquet states of ground, exciton, and biexciton states, we quantitatively reproduce the experimental observations with realistic values of exciton transition dipoles and biexciton binding energies. The result also depicts a unified physical picture of the interplay between the OSE, biexcitonic OSE and BSS in materials displaying strong many-body interactions.

## Results and discussion

### Coherent light-matter interaction

To illustrate the fundamental principle of coherent light-matter interaction, one usually considers a simplified model of a two-level ( $|g\rangle$  and  $|e\rangle$ ) system (TLS) driven by a periodic light field, whose total Hamiltonian can be expressed as<sup>5,11,15</sup>:

$$\hat{H} = \hbar\omega_{eg}\hat{c}^+\hat{c}^- + \hbar\omega_{ph}\hat{a}^+\hat{a}^- + \hbar\lambda(\hat{c}^+\hat{a}^- + \hat{c}^-\hat{a}^+) + \hbar\lambda(\hat{c}^+\hat{a}^+ + \hat{c}^-\hat{a}^-). \quad (1)$$

Here  $\omega_{eg}$  is the transition frequency of the TLS with the creation operator  $\hat{c}^+ = |e\rangle\langle g|$  and the annihilation operator  $\hat{c}^- = |g\rangle\langle e|$ ,  $\omega_{ph}$  is the photon frequency of the light field with similarly-defined operators  $\hat{a}^+$  and  $\hat{a}^-$ , and  $\lambda$  is proportional to the Rabi coupling strength containing the TLS transition dipole moment and the light field amplitude. The first and second terms in Eq. (1) correspond to the TLS and the photon reservoir, respectively. The third term is an energy conserving interaction corresponding to the OSE, whereas the last term is an

energy non-conserving one related to the BSS. Note only one-photon interactions are considered in Eq. (1); the complete form of Eq. (1) should in principle consider a ladder of all the evenly-spaced Floquet states<sup>3</sup>, but higher-order terms are typically too weak compared with the one-photon terms.

When  $\omega_{ph}$  is only slightly lower than  $\omega_{eg}$ , i.e., the energy detuning of the driving photon ( $\Delta = \hbar\omega_{eg} - \hbar\omega_{ph}$ ) is small, the last term in Eq. (1) is much weaker than the third term. This corresponds to the common situation that the magnitude of the BSS is much smaller than that of the OSE. By dropping off the last term in Eq. (1), one obtains the original formulation of the Jaynes-Cummings model<sup>16</sup>, which is also called a rotating wave approximation, and the solution of this model predicts the OSE shifts reasonably well for recent experiments<sup>4-6,8-10</sup>. When  $\omega_{ph}$  approaches zero, which can be experimentally realized by tuning the pump into infrared, the last term in Eq. (1) becomes important. However, by diagonalizing the full Hamiltonian in Eq. (1), one always obtains an energy shift as a combined result of both the OSE and BSS. Therefore, observation of an exclusive BSS, i.e., realization of the counter-rotating wave approximation, has remained intriguing for atomic/molecular and traditional solid-state systems. As mentioned in the introduction, the valley-selective transition rules in monolayer TMDs offered a unique opportunity to address this issue by separating the OSE and BSS to different valleys<sup>1</sup>.

### Spin-selectivity in lead halide perovskites

Here we choose lead halide perovskites (Fig. 1a) as the material platform for the study of BSS, because their electronic structure allows us to spin-selectively address the band-edge states using helical photons, in analogy to the valley-selectivity in monolayer TMDs. Briefly, the Bloch functions of the conduction band (CB) and valence band (VB) edges have  $p$ - and  $s$ -type symmetries<sup>17-19</sup>, respectively, which are exactly opposite to traditional II-VI and III-V group semiconductors. Therefore, there is a large spin-orbit splitting in the CB but not in the VB. The VB edge hole states have relatively pure spin states of  $m_h = \pm 1/2$ , whereas the CB edge spin-orbit split-off states are  $m_e = \pm 1/2$ ,

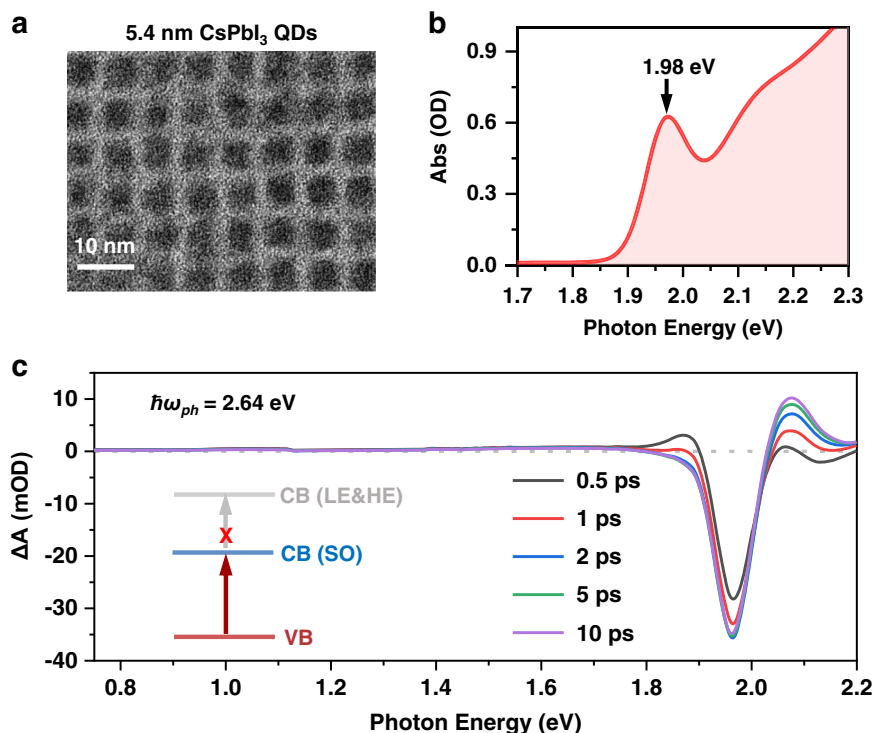


**Fig. 2 | Characterization of CsPbI<sub>3</sub> QDs.** **a** A representative transmission electron microscopy (TEM) image. **b** Steady-state absorption spectrum, with the band-edge exciton peak at -1.98 eV. **c** Broadband transient absorption (TA) spectra at varying delay times, pumped at 2.64 eV (470 nm), displaying negligible photoinduced

absorption in the near infrared region. Inset is a scheme showing the forbidden nature of the intra-CB transition from band-edge spin-orbit split-off states to higher-energy light and heavy electron states.

resulting in two optically-allowed transitions coupled to photons of opposite helicities (Fig. 1b).

With this spin-selection rule and under a quasi-particle representation, one should be able to observe the spin-exclusive OSE and BSS in CsPbI<sub>3</sub> perovskites, which are depicted in Fig. 1c, d, respectively. By coherently driving the system with a sub-bandgap photon of left-handed helicity ( $\sigma^+$ ), for example, the intragap Floquet states only interact with  $m_h = -1/2$  and  $m_e = +1/2$  states, and thus the normal OSE blueshift can be observed only with a  $\sigma^+$  probe photon (Fig. 1c), as have been reported in previous studies<sup>8–10</sup>. In contrast, the Floquet states outside the gap only interact with  $m_h = +1/2$  and  $m_e = -1/2$  states, resulting in the BSS observable only with a  $\sigma^-$  photon (Fig. 1d), which, however, has not been demonstrated yet.

We use strongly-confined CsPbI<sub>3</sub> QDs instead of bulk materials because the quantum confinement effect separates the band edge exciton from higher transitions, thereby further satisfying the approximation as a TLS. Moreover, the excitonic effects are strongly enhanced in QDs compared to bulk. Also importantly, these solution-processed QDs are uniformly dispersed in low-refractive-index solvents (here hexane), avoiding the dielectric disorder experienced by monolayer TMDs lying on substrates<sup>20</sup>. The sensitivity of the excitonic effects of monolayer TMDs to the substrates might be the reason why they are crucial in some studies but not as important in others. Thus, the perovskite QDs here are tailored to be an ideal platform to observe the BSS and to study excitonic effects on it.

### Characterization of CsPbI<sub>3</sub> perovskite QDs

The CsPbI<sub>3</sub> QDs were synthesized by a hot-injection method<sup>9,21–23</sup>. A typical transmission electron microscope (TEM) image of the CsPbI<sub>3</sub> QDs is presented in Fig. 2a, displaying cuboid-shaped QDs with an average length of ~5.4 nm. The steady-state absorption spectrum of a hexane solution of 5.4 nm QDs (Fig. 2b) reveals a sharp transition

located at 1.98 eV from the ground-state to the single-exciton state. This is considerably blueshifted compared to the bandgap of -1.8 eV for bulk CsPbI<sub>3</sub> perovskites<sup>24</sup>, a manifestation of the quantum confinement effect. Pump-probe transient absorption (TA) spectroscopy was applied to study the light-matter interactions; see details in the Methods. Figure 2c shows the TA spectra of the CsPbI<sub>3</sub> QDs acquired using linearly-polarized pump and probe beams, at pump-probe delays of a few picoseconds following an above-gap excitation ( $\hbar\omega_{ph} = 2.64$  eV). Under this condition, real exciton populations are created, inducing state-filling and Coulombic effect signals<sup>25–28</sup> much stronger than the OSE and BSS. These bleach and absorption signals are situated near the exciton energy, whereas there are negligible signals ranging from -0.7–1.7 eV as measured by our broadband probe.

In a recent study on CsPbBr<sub>3</sub> nanocrystals, a three-level system was proposed to account for anomalous Stark shifts<sup>29</sup>, in which an additional transition (at -0.8 eV) from band edge exciton state to a high-energy exciton state associated with the high-energy spin-orbit electron levels in the CB was posited. The transition dipole moment was estimated to be as large as 25 Debye. However, our direct measurement using a broad-band probe clearly rules out such a transition at least in our perovskite QDs (Fig. 2c; see also Supplementary Fig. 1), which is consistent with the forbidden nature of this intraband transition (Fig. 2c inset). This allows us to limit our discussions to the band-edge exciton states only. The high-energy excitation at 2.64 eV in Fig. 2c results in dynamic effects such as hot carrier cooling and band renormalization, which are not the focus here but can be found in previous studies<sup>30–32</sup>.

### Observation of BSS in CsPbI<sub>3</sub> perovskite QDs

To measure the OSE and BSS, we performed pump-probe experiments using circularly-polarized beams with sub-bandgap pump photon energies ( $\hbar\omega_{ph} < \hbar\omega_{eg}$ ). Presented in Fig. 3a–c are the representative TA

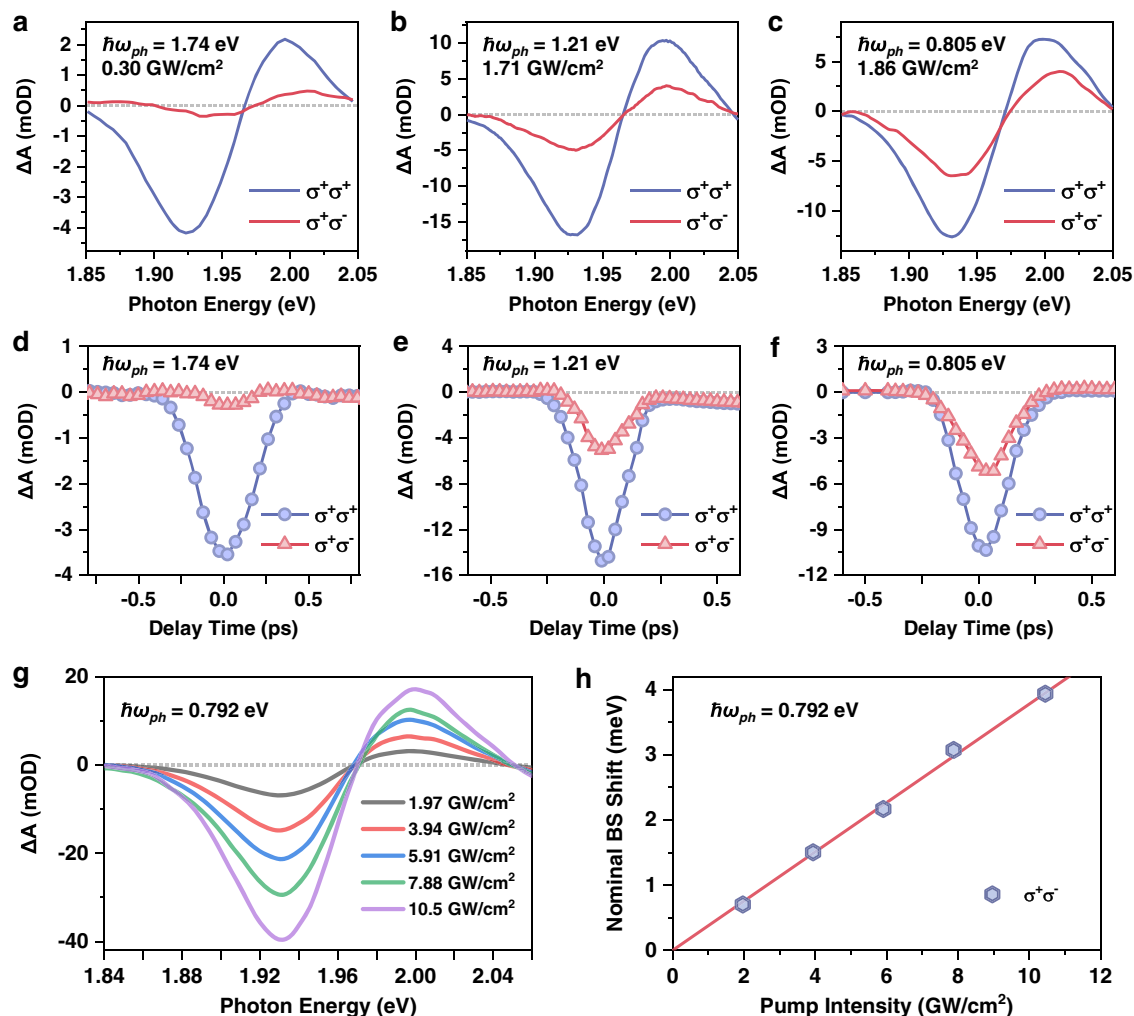


**Fig. 3 | Optical Stark ( $\sigma^+\sigma^+$ ) and Bloch-Siegert ( $\sigma^+\sigma^-$ ) shifts in CsPbI<sub>3</sub> QDs.** Time-zero transient absorption (TA) spectra obtained with  $\sigma^+\sigma^+$  (blue) and  $\sigma^+\sigma^-$  (red) pump-probe configurations with pump photon energies at (a) 1.74 eV (714 nm), (b) 1.21 eV (1027 nm), and (c) 0.805 eV (1540 nm). The incident pump intensities are indicated in each panel. **d, e, f** Temporal profiles of the signals reported in a–c. Note that the 1.74 eV pump pulse has been spectrally filtered using a grating in order to

avoid resonant excitation, and consequently the pulse duration is broadened. **g**  $\sigma^+\sigma^-$  TA spectra under varying pump intensities of 0.792 eV (1565 nm) photon. **h** Nominal Bloch-Siegert shift (blue hexagons) as a function of the incident pump intensity, calculated from the spectral-weight-transfer in **g**. The red solid line is a linear fit.

spectra of the CsPbI<sub>3</sub> QDs with  $\hbar\omega_{ph}$  of 1.74 eV (714 nm; 0.30 GW/cm<sup>2</sup>), 1.21 eV (1027 nm; 1.71 GW/cm<sup>2</sup>) and 0.805 eV (1540 nm; 1.86 GW/cm<sup>2</sup>), respectively, at time-zero. Note that because the pump intensity varies, we focus on the relative signal size of  $\sigma^+\sigma^+$  and  $\sigma^+\sigma^-$  pump-probe configurations in these plots. In contrast to Fig. 2c where it shows the real exciton population with negligible decay on the ps timescale, the signals here are not associated with any real population excitation through multiphoton absorption, as they dominate only at around time-zero when the pump and probe beams temporally overlap (Fig. 3d–f). For  $\hbar\omega_{ph} = 1.74$  eV (Fig. 3a), the detuning is relatively small ( $\Delta = 0.24$  eV), and a strong spectral modulation corresponding to the normal OSE blueshift is detected with a  $\sigma^+\sigma^+$  pump-probe configuration. In contrast, the  $\sigma^+\sigma^-$  configuration reveals a very weak spectral modulation. By decreasing  $\hbar\omega_{ph}$ , the  $\sigma^+\sigma^-$  spectral modulation progressively grows until it becomes comparable with  $\sigma^+\sigma^+$  at  $\hbar\omega_{ph} = 0.805$  eV (Fig. 3c).

The detuning-dependent behaviors observed in Fig. 3a–c are phenomenologically consistent with the spin-selective OSE and BSS of the CsPbI<sub>3</sub> QDs that we depict in Fig. 1c, d. By diagonalizing the Hamiltonian in Eq. (1) under co- and counter-rotating wave approximations, respectively, one can obtain the spectral blueshifts induced

by the pure OSE and BSS as (see Supplementary Text):

$$\begin{aligned} \delta E_{OSE} &= 2\hbar\lambda^2/(\omega_{eg} - \omega_{ph}) \\ \delta E_{BSS} &= 2\hbar\lambda^2/(\omega_{eg} + \omega_{ph}). \end{aligned} \quad (2)$$

Thus, the ratio between them is:

$$\delta E_{BSS}/\delta E_{OSE} = (\omega_{eg} - \omega_{ph})/(\omega_{eg} + \omega_{ph}), \quad (3)$$

which should increase with a decreasing  $\omega_{ph}$ , as we observed herein.

In Fig. 3g, we plot the time-zero  $\sigma^+\sigma^-$  TA spectra measured with  $\hbar\omega_{ph} = 0.792$  eV of varying power densities, which are nominally dominated by the BSS. We quantify the spectral shift using a spectral-weight-transfer calculation<sup>7</sup> and obtain power-dependent shift plotted in Fig. 3h. The signal increases linearly with the pump power, further substantiating that it is driven by single-photons. Note that the pump power was measured outside the sample cuvette, which is overestimated compared to the local power inside the QD that is screened by the solvent and QD materials. At an outside pump power of ca. 10 GW/cm<sup>2</sup>, the nominal BSS has reached 4 meV, which is several

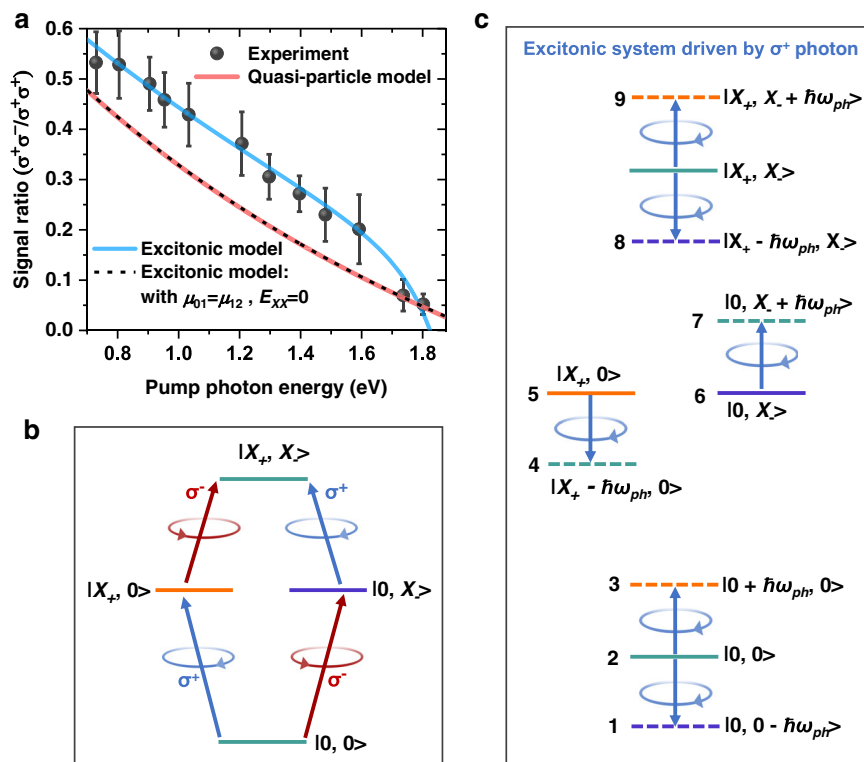


**Fig. 4 | Excitonic Bloch–Siegert shift in CsPbI<sub>3</sub> QDs. a** Ratio between the normal Bloch–Siegert and optical Stark shifts measured with  $\sigma^+\sigma^-$  and  $\sigma^+\sigma^+$  configurations, respectively (gray balls). The red solid line is the prediction by a non-interacting, quasi-particle model (Eq. (3)), whereas the blue solid line is obtained using our excitonic model (Eq. (4)) with  $\mu_{01} = 34$  D,  $\mu_{12} = 28$  D and  $E_{XX} = 65$  meV. By setting  $\mu_{01} = \mu_{12}$  and  $E_{XX} = 0$ , our excitonic model (black dashed line) reduces to the quasi-particle model. The error bars are obtained from the standard variations of  $\sigma^+\sigma^+$  and  $\sigma^+\sigma^-$  signals in the range of  $\pm 40$  fs around time-zero. **b** States and optical selection

rules under the excitonic representation. **c** Equilibrium matter states (solid lines) and Floquet states (dashed lines) driven by a nonresonant  $\sigma^+$  photon, whose angular momenta are indicated by their colors. Other Floquet states are not shown because their interactions with matter states are against angular momentum conservation. The shift of the biexciton state  $|X_+, X\rangle$  is not considered here as we are experimentally probing the shift of single-exciton transitions. There are 9 states in total in the interaction Hamiltonian.

orders of magnitude larger than those reported for superconducting-qubit TLS<sup>33,34</sup> and is comparable to the shift observed in the monolayer TMDs<sup>11</sup>. The large nominal BSS arises from the combined contribution of the small pump photon energy and the inherently strong light-matter interaction in the CsPbI<sub>3</sub> QDs.

While the BSS and OSE signals followed Eq. (2) reasonably well in ref. 11, in the presence of strong many-body excitonic effects the precision of this simple model needs to be reconsidered. This is the reason we call the shifts in Fig. 3 nominal BSS and OSE. To uncover the role of excitonic effects, we tune  $\hbar\omega_{ph}$  to 12 different energies and measure the spectral shifts under  $\sigma^+\sigma^+$  and  $\sigma^+\sigma^-$  configurations. The associated TA spectra at time-zero are presented in Supplementary Fig. 2. Quantitative comparison between our experimental results at different  $\hbar\omega_{ph}$  with Eq. (2), however, is difficult (Supplementary Fig. 3), because the pump power screening by the sample depends on  $\hbar\omega_{ph}$  and the power density measurements for different  $\hbar\omega_{ph}$  might introduce large errors. Nevertheless, by taking the ratio between the nominal  $\delta E_{BSS}$  and  $\delta E_{OSE}$ , these  $\hbar\omega_{ph}$ -dependent issues can be canceled, allowing us to compare our experimental results to Eq. (3). Figure 4a shows the plot of the ratios at 12 different  $\hbar\omega_{ph}$ , the general trend of which is in line with Eq. (3). However, the experimental ratio is systematically larger than the one predicted by Eq. (3), and the deviation is  $\hbar\omega_{ph}$ -dependent. At small detuning (e.g.,  $\hbar\omega_{ph} \sim 1.8$  eV), the deviation is small, but it becomes large as the detuning increases.

We note that a deviation from the cubic symmetry by either an orthorhombic lattice distortion or a QD shape effect can result in linearly-polarized excitons instead of circularly-polarized ones through anisotropic exchange interaction, as revealed in recent

single-particle photoluminescence studies on perovskite QDs at liquid-helium temperatures<sup>17,35,36</sup>. In this case,  $\sigma^+\sigma^+$  and  $\sigma^+\sigma^-$  configurations should yield the same signal size, i.e., the ratio between  $\sigma^+\sigma^+$  and  $\sigma^+\sigma^-$  signals should be 1 regardless the  $\hbar\omega_{ph}$  used. Even if there is only a small portion of QDs displaying such a behavior, the deviation of the experimental data from the prediction by Eq. (3) should monotonically increase with  $\hbar\omega_{ph}$ , which is just opposite to our results here. Therefore, circular-polarization selection rules still largely hold here.

A possible reason is that the anisotropy-induced exciton fine structure splitting is very weak, on the order of  $\mu\text{eV}$ – $\text{meV}$  as determined from recent single-dot<sup>17,35–37</sup> and ensemble<sup>38</sup> measurements on lead halide perovskite QDs. This splitting is much smaller in magnitude compared to the single-dot exciton linewidth of 50–100 meV for these QDs<sup>39,40</sup>. In this limit, it might still be reasonable to use the angular momentum basis of quasi-cubic approximation in Fig. 1. Indeed, when we perform linear-polarization OSE measurements for our 5.4 nm CsPbI<sub>3</sub> QDs, we find that the co- and cross-linear configurations give almost identical signal sizes (Supplementary Fig. 4). This observation is inconsistent with ideal linear-polarization selection rules which predict a signal ratio of 3:1 for co- over cross-linear configurations under orientational averaging. It is instructive to compare these results to a previous study on few-layer ReS<sub>2</sub> flakes<sup>41</sup>. Therein, the anisotropy-induced exciton splitting reaches 60 meV, much larger than the room-temperature exciton linewidth of  $\sim 25$  meV for this material, resulting in clean, linearly-polarized OSE features<sup>41</sup>. This comparison lends further support to our linewidth-versus-splitting hypothesis.



## Excitonic BSS model

To explain the observed deviation, we invoke a model taking into consideration the excitonic effects. Under an excitonic representation, the optical selection rules between the ground state  $|0, 0\rangle$ , the single-exciton states  $|X_+, 0\rangle$  and  $|0, X_-\rangle$ , and the biexciton state  $|X_+, X_-\rangle$  are depicted in Fig. 4b. When the system is coherently driven by a detuned  $\sigma^+$  photon, the six one-photon-dressed Floquet states that have strong interactions with the three equilibrium states of the ground state  $|0, 0\rangle$  and the single-exciton states  $|X_+, 0\rangle$  and  $|0, X_-\rangle$  are considered, as shown in Fig. 4c. Other Floquet states whose interactions with the single-exciton states  $|X_+, 0\rangle$  and  $|0, X_-\rangle$  are against angular momentum conservation are not included here<sup>11</sup>. The hybridizations between the states in Fig. 4c can be analyzed by diagonalizing the  $9 \times 9$  Hamiltonian:

$$\hat{H} = \begin{pmatrix} -\hbar\omega & 0 & 0 & 0 & 0 & \mu_{01}\varepsilon & 0 & 0 & 0 \\ 0 & 0 & 0 & \mu_{01}\varepsilon & 0 & 0 & \mu_{01}\varepsilon & 0 & 0 \\ 0 & 0 & \hbar\omega & 0 & \mu_{01}\varepsilon & 0 & 0 & 0 & 0 \\ 0 & \mu_{01}\varepsilon & 0 & E_1 - \hbar\omega & 0 & 0 & 0 & 0 & 0 \\ 0 & 0 & \mu_{01}\varepsilon & 0 & E_1 & 0 & 0 & 0 & \mu_{12}\varepsilon \\ \mu_{01}\varepsilon & 0 & 0 & 0 & 0 & E_1 & 0 & \mu_{12}\varepsilon & 0 \\ 0 & \mu_{01}\varepsilon & 0 & 0 & 0 & 0 & E_1 + \hbar\omega & 0 & 0 \\ 0 & 0 & 0 & 0 & 0 & \mu_{12}\varepsilon & 0 & E_2 - \hbar\omega & 0 \\ 0 & 0 & 0 & 0 & \mu_{12}\varepsilon & 0 & 0 & 0 & E_2 + \hbar\omega \end{pmatrix}. \quad (4)$$

The diagonal elements are arranged in the order of numbered states (from 1 to 9) as indicated in Fig. 4c, with the energy of  $|0, 0\rangle$  set at 0, and the energies of  $|X_+, 0\rangle$  ( $|0, X_-\rangle$ ) and  $|X_+, X_-\rangle$  at  $E_1$  and  $E_2$ , respectively.  $E_1$  and  $E_2$  are related by:  $E_2 = 2E_1 - E_{XX}$ , where  $E_{XX}$  is the biexciton interaction energy (positive for attraction). The transition dipole moment of  $|0, 0\rangle$  to  $|X_+, 0\rangle$  ( $|0, X_-\rangle$ ) is  $\mu_{01}$ , and  $|X_+, 0\rangle$  ( $|0, X_-\rangle$ ) to  $|X_+, X_-\rangle$  is  $\mu_{12}$ , which are coupled to the driving field  $\varepsilon$ .

By diagonalizing Eq. (4), we can well reproduce the experimental ratio of the nominal  $\delta E_{BSS}$  and  $\delta E_{OSE}$ , as compared in Fig. 4a. In the simulation, we use  $E_{XX} = 65$  meV,  $\mu_{01} = 34$  D, and  $\mu_{12} = 28$  D. The biexciton interaction energy results from a detailed competition between the repulsive and attractive energy parts of Coulomb and exchange interactions, which is generally attractive in low-dimensional materials<sup>42,43</sup>, unless unconventional electron and hole wavefunctions were deliberately designed<sup>44</sup>. The single-exciton transition dipole ( $\mu_{01}$ ) of 34 D is similar to the one determined from a previous OSE study of similar-size CsPbI<sub>3</sub> QDs<sup>9</sup>. The reason for a reduced magnitude of  $\mu_{12}$  than  $\mu_{01}$  is likely associated with the dielectric contrast effect for the inorganic QDs surrounded by low-refractive-index organic ligands and solvent, which enhances  $\mu_{01}$  more significantly than  $\mu_{12}$ , as predicted by a previous calculation<sup>45</sup>.

To test the generality of our model, we measured another two samples of CsPbI<sub>3</sub> QDs with average edge lengths of ~4.0 nm and 7.4 nm. The relevant data are presented in Supplementary Fig. 5. The ratio between signals obtained with  $\sigma^+\sigma^-$  and  $\sigma^+\sigma^+$  configurations ( $\sigma^+\sigma^-/\sigma^+\sigma^+$ ) for these two samples also deviate from the non-interacting, quasi-particle model, and can be well reproduced by our excitonic model. From the model fits, we obtain  $\mu_{01} = 26$  D (50 D),  $\mu_{12} = 19$  D (41 D), and  $E_{XX} = 90$  meV (48 meV) for 4.0 nm (7.4 nm) QDs; See Supplementary Table 1. Therefore, with decreasing QD size, both  $\mu_{01}$  and  $\mu_{12}$  become smaller, whereas  $E_{XX}$  is enhanced, which are consistent with the physical properties of QDs. We note that some recent studies reported repulsive biexciton interactions in lead halide perovskite QDs<sup>46–48</sup>, which are still under debate and are out of the scope of our current study. By contrast, recent single-dot PL measurements at cryogenic temperatures allow to directly readout exciton and biexciton emission lines, which gave biexciton binding energies of ~20 meV for weakly-confined (~10 nm) CsPbI<sub>3</sub> QDs<sup>36,37</sup>. These results are in line with the extrapolation of the size-dependent trend of  $E_{XX}$  obtained herein.

## Discussion

Our new model indicates that the OSE, biexcitonic OSE and BSS are partially mixed under the many-body excitonic representation. According to Fig. 4c, the key differences to the non-interacting, quasi-particle picture are: i) the ground state  $|0, 0\rangle$  is simultaneously repelled down by  $|X_+ - \hbar\omega_{ph}, 0\rangle$  and  $|0, X_- + \hbar\omega_{ph}\rangle$  through the OSE and BSS, respectively; ii) the single-exciton state  $|0, X_-\rangle$  state is repelled down by  $|X_+ - \hbar\omega_{ph}, X_-\rangle$  through the biexcitonic OSE but repelled up by  $|0, 0 - \hbar\omega_{ph}\rangle$  through the BSS; and iii) the single-exciton state  $|X_+, 0\rangle$  state is repelled up by  $|0 + \hbar\omega_{ph}, 0\rangle$  through the OSE but also repelled down by  $|X_+, X_+ + \hbar\omega_{ph}\rangle$  through the biexcitonic BBS. In the scenario of unbound biexcitons ( $\mu_{01} = \mu_{12}$  and  $E_{XX} = 0$ ), the first shift terms in i) and ii) are exactly the same, as are the second shift terms in i) and iii), and hence, the excitonic model naturally reduces to the quasi-particle model for which a spin- or valley-selective OSE or BSS can be observed. This is confirmed in our simulation in Fig. 4a. In the case of bound biexcitons, the net result of the above shifts is a generally enhanced  $\sigma^+\sigma^-/\sigma^+\sigma^+$  signal ratio. Still, there exist certain driving photon energies for which the total shifts in i) and ii) can be almost identical, thus canceling the signal in  $\sigma^+\sigma^-$  configuration. One situation in Fig. 4a is when  $\hbar\omega_{ph}$  is around 1.8–1.9 eV, i.e., the detuning is 100–200 meV. In this case, the apparent result is that a so-called spin- or valley-selective OSE can be detected (i.e.,  $\sigma^+\sigma^-$  yields a negligible shift; see the spectra in Fig. 3a for example). Indeed, detuning energies in that range were typically used in previous studies of lead halide perovskites<sup>8–10</sup> and monolayer TMDs<sup>4,5</sup> focusing on the spin- and valley-selective OSE. Further tuning  $\hbar\omega_{ph}$  towards the exciton energy should result in spectral shifts dominated by the biexcitonic OSE<sup>13,14</sup>, which however is not the focus here. Moreover, such measurements can be very challenging for our ensemble sample due to inhomogeneous broadening of the exciton linewidth, which will result in real population excitation.

To summarize, this study reports the observation of a strong Bloch–Siegert shift in CsPbI<sub>3</sub> perovskite QDs, and more importantly, it highlights the importance of many-body excitonic effects in the correct interpretation of coherent light-matter interaction even for materials with spin- or valley-selective selection rules. With these excitonic interactions, the single-exciton optical Stark effect, biexcitonic optical Stark effect and Bloch–Siegert shift are intermixed. Considering the ubiquitous role of strong excitonic effects in quantum-confined materials, the model developed here should be transferrable to many other such systems. This knowledge is crucial for the implementation of the above coherent effects to information processing and optical modulation, and to the emerging field of Floquet engineering of quantum materials<sup>49,50</sup>. Although steady-state Floquet engineering is highly desired<sup>51</sup>, these instantaneous engineering techniques in turn allow for ultrafast manipulations that are particularly useful for very high-speed quantum computing<sup>52</sup>. (*Note added in proof*: After acceptance of our manuscript, we noticed relevant studies revisiting optical Stark effect and Bloch–Siegert shift in monolayer TMDs, which also highlight the significant role of many-body effects<sup>53,54</sup>.)

## Methods

The CsPbI<sub>3</sub> QDs were synthesized via a hot-injection method described elsewhere<sup>22</sup>. Pump-probe measurements were conducted using a Pharos Yb: KGW laser (Light Conversion; 1030 nm, 230 fs pulse-duration, 100 kHz repetition rate) as the laser source. The output laser was split into multiple beams, one of which was directed to an optical parametric amplifier (Orpheus-HP; Light Conversion) to generate wavelength-tunable pump pulses, and the other being delayed by a motorized delay stage and then focused onto a YAG crystal to generate a white light continuum as the

probe. In order to eliminate the potential polarization distortion during the propagation of beams, circular polarization of pump and probe beams was produced by separately inserting two sets of beam-splitting cubes (Thorlabs) and quarter-wave plates (Thorlabs) right before the sample. The pump and probe directions were set to a small crossing angle at  $-6^\circ$ , and focused onto the sample with long focal lens of 40 and 25 cm, respectively. For all the detuned pump laser wavelengths, the sizes of the foci on the sample were measured to be in the range 250–300  $\mu\text{m}$ , more than twice larger than the probe beam size ( $\sim 120 \mu\text{m}$ ). The transmitted probe beam was re-collimated and focused into a fiber-coupled spectrometer to record the variation in absorbance of the sample induced by pump pulses. The sample was placed into a 1 mm quartz cuvette and all measurements were carried out at room temperature ( $\sim 298 \text{ K}$ ).

### Data availability

All data is available in the main text or the supplementary Information and can be obtained upon request from K.W. (kwu@dicp.ac.cn). They are also available at figshare, <https://figshare.com/articles/figure/Figures-final-BSS/21076276>. Source data are provided with this paper.

### Code availability

Custom software developed for theoretical modeling associated with this study is available for verification purposes upon request from J.Z (jingyizh@dicp.ac.cn), but is not provided here due to its highly custom-made nature.

### References

1. Autler, S. H. & Townes, C. H. Stark effect in rapidly varying fields. *Phys. Rev.* **100**, 703–722 (1955).
2. Bloch, F. & Siegert, A. Magnetic resonance for nonrotating fields. *Phys. Rev.* **57**, 522–527 (1940).
3. Shirley, J. H. Solution of the Schrödinger equation with a hamiltonian periodic in time. *Phys. Rev.* **138**, B979–B987 (1965).
4. Kim, J. et al. Ultrafast generation of pseudo-magnetic field for valley excitons in WSe<sub>2</sub> monolayers. *Science* **346**, 1205 (2014).
5. Sie, E. J. et al. Valley-selective optical Stark effect in monolayer WS<sub>2</sub>. *Nat. Mater.* **14**, 290–294 (2015).
6. Cunningham, P. D., Hanbicki, A. T., Reinecke, T. L., McCreary, K. M. & Jonker, B. T. Resonant optical Stark effect in monolayer WS<sub>2</sub>. *Nat. Commun.* **10**, 5539 (2019).
7. Yong, C.-K. et al. Valley-dependent exciton fine structure and Autler–Townes doublets from Berry phases in monolayer MoSe<sub>2</sub>. *Nat. Mater.* **18**, 1065–1070 (2019).
8. Yang, Y. et al. Large polarization-dependent exciton optical Stark effect in lead iodide perovskites. *Nat. Commun.* **7**, 12613 (2016).
9. Li, Y., He, S., Luo, X., Lu, X. & Wu, K. Strong spin-selective optical Stark effect in lead halide perovskite quantum dots. *J. Phys. Chem. Lett.* **11**, 3594–3600 (2020).
10. Giovanni, D. et al. Tunable room-temperature spin-selective optical Stark effect in solution-processed layered halide perovskites. *Sci. Adv.* **2**, e1600477 (2016).
11. Sie, E. J. et al. Large, valley-exclusive Bloch–Siegert shift in monolayer WS<sub>2</sub>. *Science* **355**, 1066 (2017).
12. Sie, E. J., Lui, C. H., Lee, Y.-H., Kong, J. & Gedik, N. Observation of intervalley biexcitonic optical Stark effect in monolayer WS<sub>2</sub>. *Nano Lett.* **16**, 7421–7426 (2016).
13. Yong, C.-K. et al. Biexcitonic optical Stark effects in monolayer molybdenum diselenide. *Nat. Phys.* **14**, 1092–1096 (2018).
14. Shrivastava, M. et al. Room-temperature anomalous coherent excitonic optical Stark effect in metal halide perovskite quantum dots. *Nano Lett.* **22**, 808–814 (2022).
15. Schmitt, H. A. & Mufti, A. Two-level Jaynes–Cummings Hamiltonian as a supersymmetric quantum-mechanical system. *Phys. Rev. D.* **43**, 2743–2744 (1991).
16. Jaynes, E. T. & Cummings, F. W. Comparison of quantum and semiclassical radiation theories with application to the beam maser. *Proc. IEEE* **51**, 89–109 (1963).
17. Becker, M. A. et al. Bright triplet excitons in caesium lead halide perovskites. *Nature* **553**, 189–193 (2018).
18. Even, J., Pedesseau, L., Jancu, J.-M. & Katan, C. Importance of spin–orbit coupling in hybrid organic/inorganic perovskites for photovoltaic applications. *J. Phys. Chem. Lett.* **4**, 2999–3005 (2013).
19. Huang, L.-y & Lambrecht, W. R. L. Electronic band structure, phonons, and exciton binding energies of halide perovskites CsSnCl<sub>3</sub>, CsSnBr<sub>3</sub>, and CsSnI<sub>3</sub>. *Phys. Rev. B* **88**, 165203 (2013).
20. Raja, A. et al. Dielectric disorder in two-dimensional materials. *Nat. Nanotechnol.* **14**, 832–837 (2019).
21. Protesescu, L. et al. Nanocrystals of Cesium Lead Halide Perovskites (CsPbX<sub>3</sub>, X = Cl, Br, and I): novel optoelectronic materials showing bright emission with wide color gamut. *Nano Lett.* **15**, 3692–3696 (2015).
22. Li, Y., Luo, X., Ding, T., Lu, X. & Wu, K. Size- and halide-dependent Auger recombination in lead halide perovskite nanocrystals. *Angew. Chem. Int. Ed.* **59**, 14292–14295 (2020).
23. Dong, Y. et al. Precise control of quantum confinement in cesium lead halide perovskite quantum dots via thermodynamic equilibrium. *Nano Lett.* **18**, 3716–3722 (2018).
24. Yang, Z. et al. Impact of the halide cage on the electronic properties of fully inorganic cesium lead halide perovskites. *ACS Energy Lett.* **2**, 1621–1627 (2017).
25. Rossi, D. et al. Light-induced activation of forbidden exciton transition in strongly confined perovskite quantum dots. *ACS Nano* **12**, 12436–12443 (2018).
26. Shang, Q., Kaledin, A. L., Li, Q. & Lian, T. Size dependent charge separation and recombination in CsPbI<sub>3</sub> perovskite quantum dots. *J. Chem. Phys.* **151**, 074705 (2019).
27. Makarov, N. S. et al. Spectral and dynamical properties of single excitons, biexcitons, and trions in cesium–lead–halide perovskite quantum dots. *Nano Lett.* **16**, 2349–2362 (2016).
28. Wu, K. et al. Ultrafast interfacial electron and hole transfer from CsPbBr<sub>3</sub> perovskite quantum dots. *J. Am. Chem. Soc.* **137**, 12792–12795 (2015).
29. Yumoto, G. et al. Strong spin-orbit coupling inducing Autler–Townes effect in lead halide perovskite nanocrystals. *Nat. Commun.* **12**, 3026 (2021).
30. de Weerd, C. et al. Efficient carrier multiplication in CsPbI<sub>3</sub> perovskite nanocrystals. *Nat. Commun.* **9**, 4199 (2018).
31. Yu, B. et al. Size-dependent hot carrier dynamics in perovskite nanocrystals revealed by two-dimensional electronic spectroscopy. *J. Phys. Chem. Lett.* **12**, 238–244 (2021).
32. Saran, R., Heuer-Jungemann, A., Kanaras, A. G. & Curry, R. J. Giant bandgap renormalization and exciton–phonon scattering in perovskite nanocrystals. *Adv. Opt. Mater.* **5**, 1700231 (2017).
33. Forn-Díaz, P. et al. Observation of the Bloch–Siegert shift in a qubit-oscillator system in the ultrastrong coupling regime. *Phys. Rev. Lett.* **105**, 237001 (2010).
34. Tuorila, J. et al. Stark effect and generalized Bloch–Siegert shift in a strongly driven two-level system. *Phys. Rev. Lett.* **105**, 257003 (2010).
35. Tamarat, P. et al. The ground exciton state of formamidinium lead bromide perovskite nanocrystals is a singlet dark state. *Nat. Mater.* **18**, 717–724 (2019).
36. Yin, C. et al. Bright-exciton fine-structure splittings in single perovskite nanocrystals. *Phys. Rev. Lett.* **119**, 026401 (2017).

37. Tamarat, P. et al. The dark exciton ground state promotes photon-pair emission in individual perovskite nanocrystals. *Nat. Commun.* **11**, 6001 (2020).
38. Han, Y. et al. Lattice distortion inducing exciton splitting and coherent quantum beating in CsPbI<sub>3</sub> perovskite quantum dots. *Nat. Mater.* <https://doi.org/10.1038/s41563-022-01349-4> (2022).
39. Park, Y.-S., Guo, S., Makarov, N. S. & Klimov, V. I. Room temperature single-photon emission from individual perovskite quantum dots. *ACS Nano* **9**, 10386–10393 (2015).
40. Utzat, H. et al. Probing linewidths and biexciton quantum yields of single cesium lead halide nanocrystals in solution. *Nano Lett.* **17**, 6838–6846 (2017).
41. Sim, S. et al. Selectively tunable optical Stark effect of anisotropic excitons in atomically thin ReS<sub>2</sub>. *Nat. Commun.* **7**, 13569 (2016).
42. Grim, J. Q. et al. Continuous-wave biexciton lasing at room temperature using solution-processed quantum wells. *Nat. Nanotechnol.* **9**, 891–895 (2014).
43. You, Y. et al. Observation of biexcitons in monolayer WSe<sub>2</sub>. *Nat. Phys.* **11**, 477–481 (2015).
44. Klimov, V. I. et al. Single-exciton optical gain in semiconductor nanocrystals. *Nature* **447**, 441–446 (2007).
45. Takagahara, T. Biexciton states in semiconductor quantum dots and their nonlinear optical properties. *Phys. Rev. B* **39**, 10206–10231 (1989).
46. Ashner, M. N. et al. Size-dependent biexciton spectrum in CsPbBr<sub>3</sub> perovskite nanocrystals. *ACS Energy Lett.* **4**, 2639–2645 (2019).
47. Dana, J., Binyamin, T., Etgar, L. & Ruhman, S. Unusually strong biexciton repulsion detected in quantum confined CsPbBr<sub>3</sub> nanocrystals with two and three pulse femtosecond spectroscopy. *ACS Nano* **15**, 9039–9047 (2021).
48. Lubin, G. et al. Resolving the controversy in biexciton binding energy of cesium lead halide perovskite nanocrystals through heralded single-particle spectroscopy. *ACS Nano* **15**, 19581–19587 (2021).
49. Wang, Y. H., Steinberg, H., Jarillo-Herrero, P. & Gedik, N. Observation of Floquet-Bloch states on the surface of a topological insulator. *Science* **342**, 453–457 (2013).
50. Oka, T. & Kitamura, S. Floquet engineering of quantum materials. *Annu. Rev. Cond. Matt. Phys.* **10**, 387–408 (2019).
51. Park, S. et al. Steady Floquet–Andreev states in graphene Josephson junctions. *Nature* **603**, 421–426 (2022).
52. Boolakee, T. et al. Light-field control of real and virtual charge carriers. *Nature* **605**, 251–255 (2022).
53. Slobodeniuk, A. et al. Giant valley-selective Stark and Bloch-Siegert shifts of exciton resonances in WSe<sub>2</sub> and MoS<sub>2</sub> monolayers. Preprint at <https://arxiv.org/abs/2204.00842> (2022).
54. Slobodeniuk, A. et al. Semiconductor Bloch equation analysis of optical Stark and Bloch-Siegert shifts in monolayers WSe<sub>2</sub> and MoS<sub>2</sub>. Preprint at <https://arxiv.org/abs/2204.00836> (2022).

## Acknowledgements

K.W. acknowledges financial support from the Chinese Academy of Sciences (YSBR-007), the Ministry of Science and Technology of China (2018YFA0208703), the National Natural Science Foundation of China (22173098) and Dalian Institute of Chemical Physics (DICP I201914). K.W. also thanks Dr. Peter C. Sercel for useful discussions on exciton polarizations.

## Author contributions

K.W. supervised the study and designed the project. Y.H., Yux.L. and W.L. synthesized the samples. Yux.L. and J.Z. measured their spectroscopy. J.Z. developed the Hamiltonian for the simulation. B.Z., Yul.L., Yua.L. and Y.Y. helped with sample synthesis or spectroscopy experiments. K.W. and J.Z. wrote the manuscript with contributions from all authors.

## Competing interests

The authors declare no competing interests.

## Additional information

**Supplementary information** The online version contains supplementary material available at <https://doi.org/10.1038/s41467-022-33314-9>.

**Correspondence** and requests for materials should be addressed to Kaifeng Wu or Jingyi Zhu.

**Peer review information** *Nature Communications* thanks Giulio Cerullo and the other, anonymous, reviewers for their contribution to the peer review of this work.

**Reprints and permission information** is available at <http://www.nature.com/reprints>

**Publisher's note** Springer Nature remains neutral with regard to jurisdictional claims in published maps and institutional affiliations.

**Open Access** This article is licensed under a Creative Commons Attribution 4.0 International License, which permits use, sharing, adaptation, distribution and reproduction in any medium or format, as long as you give appropriate credit to the original author(s) and the source, provide a link to the Creative Commons license, and indicate if changes were made. The images or other third party material in this article are included in the article's Creative Commons license, unless indicated otherwise in a credit line to the material. If material is not included in the article's Creative Commons license and your intended use is not permitted by statutory regulation or exceeds the permitted use, you will need to obtain permission directly from the copyright holder. To view a copy of this license, visit <http://creativecommons.org/licenses/by/4.0/>.

© The Author(s) 2022